

Supplementary Information

Optofluidic Lasers with Monolayer Gain at the Liquid-Liquid Interface

Han Zhang^a, Anirudh Balram^b, Dennis Desheng Meng^b, and Yuze Sun^{a*}

^aDepartment of Electrical Engineering, University of Texas at Arlington
Arlington, TX 76019

^bDepartment of Mechanical Engineering, University of Texas at Arlington
Arlington, TX 76019

*sun@uta.edu

I. Superhydrophilic surface formation by electrodeposition

The inherent wetting nature of a surface is dictated by its surface free energy and can be further amplified by an increase in surface roughness.¹ Surface wettability is typically characterized by the water contact angle (WCA) on a surface. For example, transition metal hydroxides² and oxides such as Ni(OH)_2 , Co(OH)_2 , NiO , Co_3O_4 , *etc.* are inherently hydrophilic ($\text{WCA} < 90^\circ$) in nature. Introducing hierarchical micro/nano roughness further amplifies the hydrophilicity leading to the extreme wetting state of superhydrophilicity ($\text{WCA} < 5^\circ$). The extremely high water affinity of such a surface can be utilized to achieve a corresponding underwater superoleophobic state,³ *i.e.* the state of extreme repellence of a surface towards oil when in an aqueous medium. When immersed in water, the hierarchical structures of the superhydrophilic surface are entirely infiltrated and prevent oil droplet adhesion to the surface by drastically minimizing contact area. One convenient way to prepare such underwater superoleophobic surfaces⁴ is through electrodeposition, where the morphology of the deposited materials can be controlled by fine tuning of the deposition parameters such as the bath composition, pH, deposition voltage, current density, *etc.*⁵

We use electrodeposition in order to produce superhydrophilic nickel cobalt hydroxide deposits with hierarchical micro/nano structures. The electrodeposits were produced in a primarily ethanol and isopropanol based medium with $\sim 2\%$ added volume of deionized water. A total of 0.1 mg/ml of $\text{NiCl}_2 \cdot 6\text{H}_2\text{O}$ and $\text{CoCl}_2 \cdot 6\text{H}_2\text{O}$ in a 1:1 ratio were dissolved into the solution to prepare the deposition bath. Deposition was carried out for 3 min at ~ 250 V/cm using a Matsusada high-voltage power source (Model EJ-2R100). Deposits were typically made on FTO glass substrates using a graphite foil counter electrode. Contact angle characterization images were analyzed by implementing the LB-ADSA plugin in ImageJ.⁶

II. Oil droplet generation

Oil droplets are generated following the standard protocol.⁷⁻⁸ The T-junction (MicroTee P-890, IDEX) is connected to two input microfluidic channels (150 μm in diameter) and one output channel (197 μm in diameter). Aqueous phase and oil phase are injected into two input channels, respectively, using syringe pumps (70-2202, Harvard Apparatus). The flow rate of aqueous phase and oil phase are 900 $\mu\text{L}/\text{min}$ and 50 $\mu\text{L}/\text{min}$, respectively. The droplet size distribution generated is shown in **Fig. S1**. The majority of the droplets has a diameter in the range of 100 μm to 145 μm .

III. Lasing performance of Nile Red microdroplets

Lasing emission spectra of oil microdroplets with different concentrations of Nile Red are shown in **Fig. S2(a)**. The diameter of oil microdroplets is 123 ± 11 μm . When the concentration of Nile Red is decreased from 1 mM to 7.5 μM , the lasing emission wavelengths shift to shorter wavelength. The lasing spectrum central position changes from 645 nm (1 mM Nile Red droplets) to 625 nm (7.5 μM Nile Red droplets). **Fig. S2(b)** shows the integrated lasing emission intensity as a function of the pump energy density for different dye concentrations. Their respective lasing thresholds are provided in the caption of **Fig. S2**.

IV. Theoretical analysis of microdroplet dye lasers

Both Dil(3) and Nile Red microdroplet lasers can be modeled as the four-energy-level laser system. The corresponding population inversion condition can be written as:⁹⁻¹¹

$$n_1 \sigma_e(\lambda_L) \geq (n_T - n_1) \sigma_a(\lambda_L) + \frac{2\pi m}{\lambda_L Q_0} \quad (\text{S1})$$

where n_T is the total concentration of the dye, n_l is the concentration of the dye in the excited state, $\sigma_e(\lambda_L)$ ($\sigma_a(\lambda_L)$) is the dye emission cross-section (dye absorption cross-section) at the lasing wavelength λ_L , Q_0 is the microdroplet empty-cavity Q-factor, and m is the effective refractive index of the WGMs. At threshold, Eq. (S1) can be written as:

$$\gamma = \frac{\sigma_a(\lambda_L)}{\sigma_e(\lambda_L) + \sigma_a(\lambda_L)} \left[1 + \frac{Q_{abs}}{Q_0} \right] \quad (S2)$$

where

$$Q_{abs} = \frac{2\pi m}{\lambda_L n_l \sigma_a(\lambda_L)} \quad (S3)$$

is the Q-factor related to the dye absorption. $\gamma \equiv n_l / n_t$ is the fraction of gain molecules in the excited state at the threshold.

According to the laser theory, the lasing threshold, I_{th} , is determined by:

$$I_{th} = \frac{\gamma}{1 - \gamma} \quad (S4)$$

To solve lasing threshold according to Eqs. (S2) - (S4), the dye absorption cross-section and the dye emission cross-section at the lasing wavelength are measured in the experiments detailed below in Section VI and VIII, respectively.

The crucial difference between Dil(3) microdroplet laser and Nile Red microdroplet laser lies in the gain medium spatial distribution. In Nile Red laser, dye molecules are homogeneously distributed in the microdroplet, as in the majority of dye lasers reported to date. However, since Dil(3) molecules are amphiphilic, which behaves like a surfactant, they will diffuse to and form a monolayer at the microdroplet surface first. Any additional dye molecules will then homogeneously distributed in the entire volume of the droplet. Therefore, the total concentration

of the dye participating lasing (n_T) in Dil(3) laser needs to be corrected based on the following two cases.

In a droplet microcavity, WGMs form at the droplet surface (*i.e.*, liquid-liquid interface in droplet lasers described in our work) through continuous total internal reflections and is confined inside of the droplet. Assume that WGMs spatial distribution occupies a layer with a thickness of $d_{WGMs} \sim (\lambda_L/n)$ from the droplet liquid-liquid interface. When a complete monolayer of Dil(3) is formed at the surface and there is no free dye molecules in the droplet, the total number of Dil(3) molecules are:

$$N = \frac{S}{IMD^2} = \frac{4\pi R^2}{IMD^2} \quad (S5)$$

where S is the surface area of the droplet, R is the radius of the droplet, and IMD is the intermolecular distance between two adjacent Dil(3) molecules on the surface. Therefore the corresponding dye concentration in the droplet is written as:

$$C_c = \frac{N}{V} = \frac{N}{\frac{4}{3}\pi R^3} \quad (S6)$$

where V is the volume of the droplet. C_c is defined as the critical concentration, where the number of Dil(3) molecules in the bulk solution is just enough to form a monolayer gain at the droplet surface and there is no free dye molecules left in the solution. When the bulk concentration is smaller than the critical concentration ($c < C_c$), the effective gain medium concentration experienced by the WGMs is

$$n_T(c) = \frac{V \cdot c}{V_{WGMs}} \quad (S7)$$

where $V_{WGMs} = V - \frac{4}{3}\pi(R - d_{WGMs})^3 \quad (S8)$

When the bulk concentration is larger than the critical concentration ($c > C_c$), the effective gain medium concentration experienced by the WGMs is

$$n_T(c) = c + \left(\frac{1}{V_{WGMs}} - \frac{1}{V} \right) N \quad (S9)$$

In Dil(3) microdroplet laser, the critical concentration and effective concentration are dependent on droplet size, as shown in **Fig. S3**.

For Nile Red microdroplet laser, the total concentration of the dye participating lasing (n_T) is always equal to bulk solution concentration (c) in the droplet.

V. Fluorescence lifetime measurement

A custom-built fluorescence lifetime measurement system¹² is used to characterize the lifetime of Dil(3) and Nile Red. Briefly, laser light of 500 nm with a pulse width of ~800 ps is used to excite the sample. The fluorescence emission is detected by a photomultiplier tube (H10721-20, Hamamatsu). The signal is further amplified by a broadband preamplifier (C5594, Hamamatsu) and then acquired by a multi-channel oscilloscope (DPO 7254, Tektronix). The system response is measured by using the pure immersion oil as a control sample and is used to deconvolve the acquired fluorescence decay data from Dil(3) and Nile Red, respectively. The processed data is then fitted to a mono-exponential decay function to extract the lifetime value. According to the results shown in **Fig. S4**, the fluorescence lifetime of Dil(3) and Nile Red are 2.11 ns and 3.99 ns, respectively.

VI. Absorption cross-section measurement

A custom-built absorbance measurement setup is used to characterize the dye absorption cross-section. A tungsten halogen light source (HL-2000, Ocean Optics) is used to excite the sample placed in standard quartz cuvette and the fluorescence emission spectrum is measured with a spectrometer (HR 4000, Ocean Optics). The absorbance spectra of 7.5 μM Dil(3) and 7.5 μM Nile Red, $A(\lambda)$, are measured respectively. Absorption cross-section, $\sigma_a(\lambda)$, is calculated based on equation:

$$\sigma_a(\lambda) = \frac{-[\ln(10^{-A(\lambda)})]}{n(\text{molecules}/\text{cm}^3) \cdot l(\text{cm})} = [\text{cm}^2/\text{molecule}] \quad (\text{S10})$$

where l is the length of light path, n is the concentration of dye, and A is the absorbance. The absorption cross-section is shown in **Fig. S5**. The absorption cross-section values beyond 600 nm is obtained through Gaussian fitting extrapolation.

VII. Quantum yield measurement

To determine the quantum yield of Dil(3) and Nile Red, we measured the absorbance and fluorescence of both dyes (in immersion oil) in parallel with Rhodamine 6G (R6G) (in methanol). The absorbance and fluorescence tests are performed with Infinite M-200 (Tecan). The excitation (or absorption) wavelength is fixed at 500 nm. The experimental results are shown in **Fig. S6**. Based on **Table. S1**, the quantum yield can be calculated using equation:

$$\Phi_s = \Phi_{ref} \times \frac{FL - slope_s}{FL - slope_{ref}} \times \frac{RI_s^2}{RI_{ref}^2} \times \frac{\epsilon_{ref}}{\epsilon_s} \quad (\text{S11})$$

where Φ is the quantum yield, RI is the refractive index of the solvent, $FL-slope$ is the fluorescence efficiency, and ϵ is the extinction coefficient. We calculate that $\Phi_{Dil3} = 0.33$ and $\Phi_{NileRed} = 0.79$ ($\Phi_{ref} = \Phi_{R6G} = 0.93$ for R6G in methanol¹³).

VIII. Fluorescence quantum distribution and emission cross-section calculation

Based on the emission spectra and Gaussian fit shown in **Fig. S7**, and the fluorescence quantum yield of Dil(3) and Nile Red ($\Phi_{Dil(3)} = 0.33$, $\Phi_{Nile Red} = 0.78$), Dil(3) fluorescence quantum distribution at 618 nm and Nile Red fluorescence quantum distribution at 635 nm are calculated as below:

$$E(\lambda_L) = \frac{\Phi}{w\sqrt{2\pi}} \exp\left[-\frac{(\lambda_L - \lambda_0)^2}{2w^2}\right] \quad (S12)$$

where $E(\lambda_L)$ is the fluorescence quantum distribution, and λ_0 and w are the center wavelength and standard deviation of the Gaussian fit. From the results obtained in **Fig. S7**, $w_{Dil(3)} = 40.45$ nm, $w_{Nile Red} = 43.16$ nm, $\lambda_{0,Dil(3)} = 578$ nm, and $\lambda_{0,NileRed} = 610$ nm, respectively.

Therefore,

$$E(618nm)_{Dil3} = \frac{0.33}{40.45nm\sqrt{2\pi}} \exp\left[-\frac{(618-578)^2}{2 \times 40.45^2}\right] = 2 \cdot 10^{-3} nm^{-1}$$

$$E(635nm)_{NileRed} = \frac{0.79}{43.16nm\sqrt{2\pi}} \exp\left[-\frac{(635-610)^2}{2 \times 43.16^2}\right] = 6.2 \cdot 10^{-3} nm^{-1}$$

According to the following equation:¹⁴

$$\sigma_e(\lambda_L) = \frac{\lambda_L^4 \cdot E(\lambda_L)}{8\pi \cdot c \cdot n_L^2 \tau_F} \quad (S13)$$

where n_L is the medium refractive index at λ_L , and c is the speed of light in a vacuum. Using experimentally measured data as detailed previously, the emission cross-section of Dil(3) at 618 nm is estimated to be $\sigma_e(\lambda_L) = 7.98 \times 10^{-17} \text{ cm}^2$ and the emission cross-section of Nile Red at 635 nm is estimated to be $\sigma_e(\lambda_L) = 1.46 \times 10^{-16} \text{ cm}^2$.

References

1. Balram, A.; Santhanagopalan, S.; Hao, B.; Yap, Y. K.; Meng, D. D. Electrophoretically-Deposited Metal-Decorated CNT Nanoforests with High Thermal/Electric Conductivity and Wettability Tunable from Hydrophilic to Superhydrophobic. *Adv. Funct. Mater.* **2016**, *26*, 2571-2579.
2. Dubal, D.; Jagadale, A.; Patil, S.; Lokhande, C. Simple route for the synthesis of supercapacitive Co–Ni mixed hydroxide thin films. *Mater. Res. Bull.* **2012**, *47*, 1239-1245.
3. Yong, J.; Yang, Q.; Chen, F.; Bian, H.; Du, G.; Farooq, U.; Hou, X. Reversible Underwater Lossless Oil Droplet Transportation. *Adv. Mater. Interfaces* **2015**, *2*, 1400388.
4. Manna, U.; Lynn, D. M. Synthetic Surfaces with Robust and Tunable Underwater Superoleophobicity. *Adv. Funct. Mater.* **2015**, *25*, 1672-1681.
5. Chang, Y.-H.; Huang, Y.-T.; Lo, M. K.; Lin, C.-F.; Chen, C.-M.; Feng, S.-P. Electrochemical fabrication of transparent nickel hydroxide nanostructures with tunable superhydrophobicity/superhydrophilicity for 2D microchannels application. *J. Mater. Chem. A* **2014**, *2*, 1985-1990.
6. Stalder, A. F.; Melchior, T.; Müller, M.; Sage, D.; Blu, T.; Unser, M. Low-bond axisymmetric drop shape analysis for surface tension and contact angle measurements of sessile drops. *Colloids Surf., A* **2010**, *364*, 72-81.
7. Garstecki, P.; Fuerstman, M. J.; Stone, H. A.; Whitesides, G. M. Formation of droplets and bubbles in a microfluidic T-junction - scaling and mechanism of break-up. *Lab Chip* **2006**, *6*, 437-446.
8. Wang, K.; Lu, Y.; Xu, J.; Luo, G. Determination of dynamic interfacial tension and its effect on droplet formation in the T-shaped microdispersion process. *Langmuir* **2009**, *25*, 2153-2158.
9. Lacey, S.; White, I. M.; Sun, Y.; Shopova, S. I.; Cupps, J. M.; Zhang, P.; Fan, X. Versatile opto-fluidic ring resonator lasers with ultra-low threshold. *Opt. Express* **2007**, *15*, 15523-15530.
10. Moon, H.-J.; Chough, Y.-T.; An, K. Cylindrical microcavity laser based on the evanescent-wave-coupled gain. *Phys. Rev. Lett.* **2000**, *85*, 3161.
11. Sun, Y.; Fan, X. Distinguishing DNA by Analog-to-Digital-like Conversion by Using Optofluidic Lasers. *Angew. Chem. Int. Ed.* **2012**, *51*, 1236-1239.
12. Saremi, B.; Wei, M.-Y.; Liu, Y.; Cheng, B.; Yuan, B. Re-evaluation of biotin-streptavidin conjugation in Förster resonance energy transfer applications. *BIOMEDO* **2014**, *19*, 085008.
13. Magde, D.; Wong, R.; Seybold, P. G. Fluorescence quantum yields and their relation to lifetimes of rhodamine 6G and fluorescein in nine solvents: improved absolute standards for quantum yields. *Photochem. Photobiol.* **2002**, *75*, 327-334.
14. Deshpande, A.; Beidoun, A.; Penzkofer, A.; Wagenblast, G. Absorption and emission spectroscopic investigation of cyanovinyldiethylaniline dye vapors. *Chem. Phys* **1990**, *142*, 123-131.

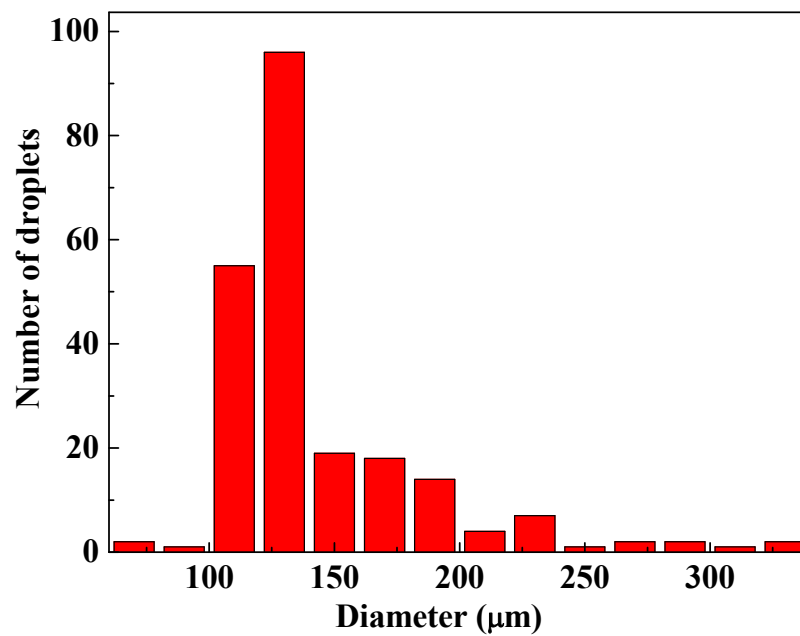


Fig. S1 Size distribution of oil droplets generated by a T-junction.

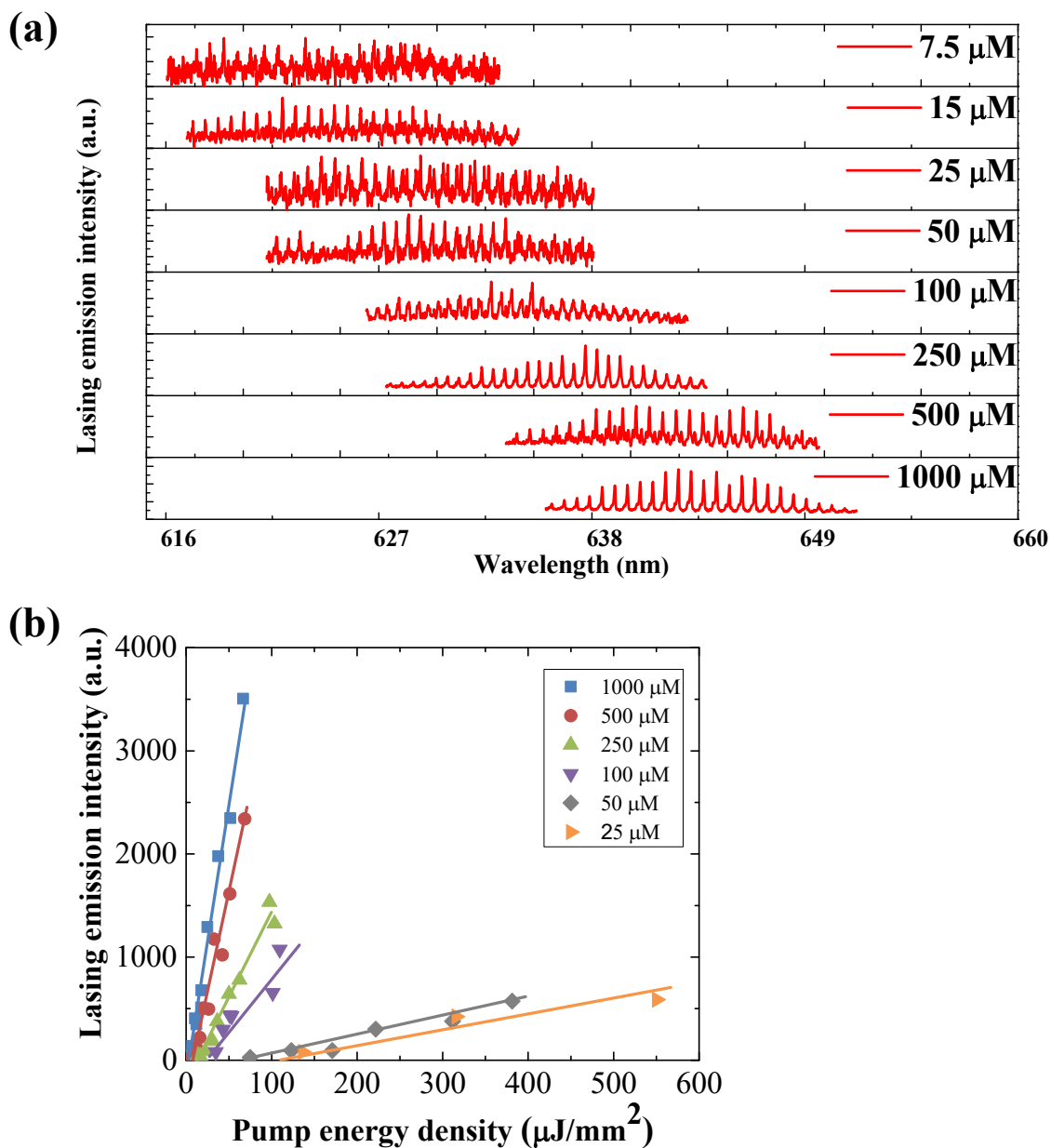


Fig. S2 (a) Lasing spectra of oil droplets with different concentrations of Nile Red (from 7.5 mM to 1 mM), pumped well-above threshold. Excitation wavelength: 532 nm. (b) Lasing threshold curves of oil droplets with different concentrations of Nile Red. The threshold for each concentration in increasing order is 111 $\mu\text{J}/\text{mm}^2$, 68 $\mu\text{J}/\text{mm}^2$, 27 $\mu\text{J}/\text{mm}^2$, 14 $\mu\text{J}/\text{mm}^2$, 8 $\mu\text{J}/\text{mm}^2$, and 4 $\mu\text{J}/\text{mm}^2$, respectively.

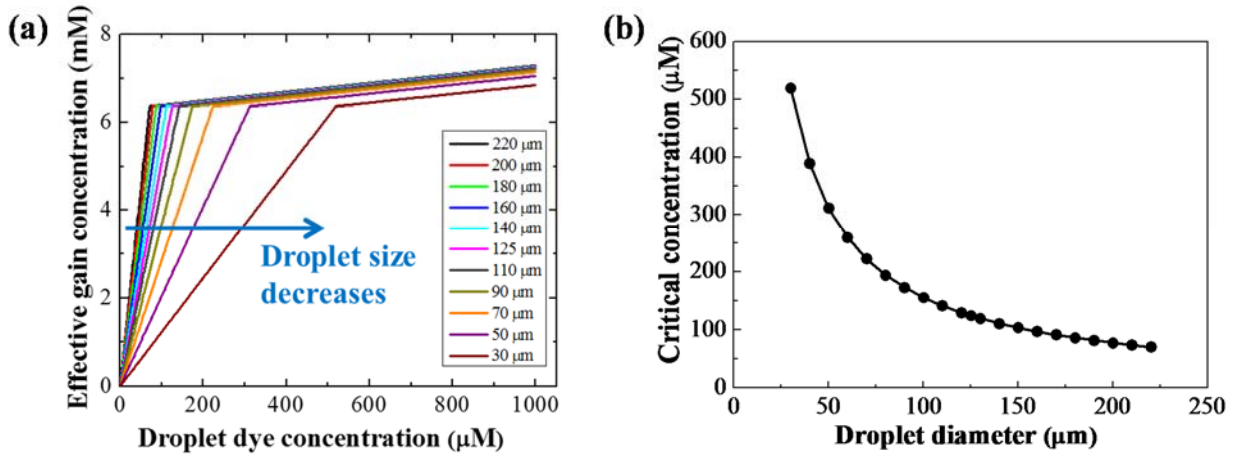


Fig. S3 Dil(3) microdroplet laser size dependence. (a) Effective gain concentration for different sizes of droplets (droplets diameter vary from 30 to 220 μm). (b) Relation between critical concentration and droplet size.

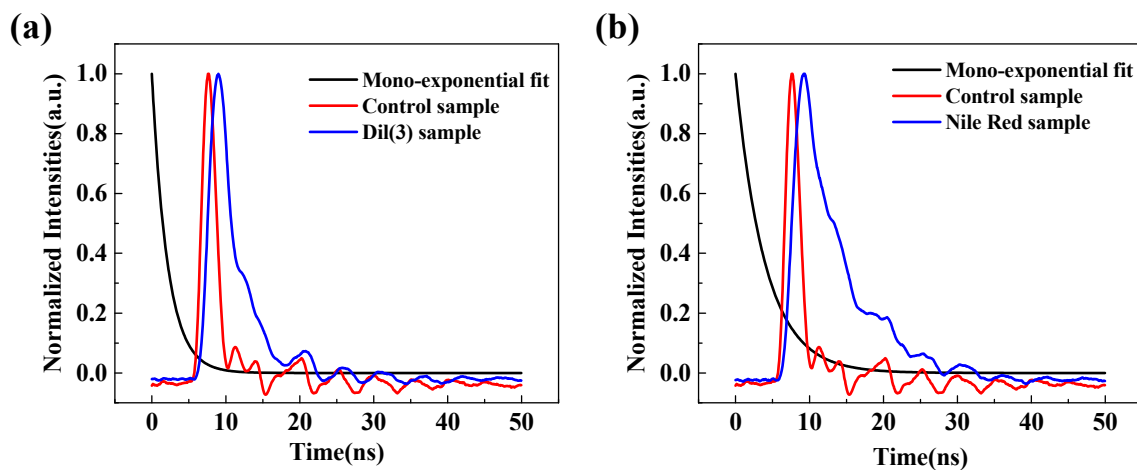


Fig. S4 Fluorescence lifetime measurement. Fluorescence decay curves of 10 μM Dil(3) in mineral oil and 10 μM Nile Red in mineral oil are shown in (a) and (b), respectively. Control shows system response obtained with pure immersion oil. Mono-exponential fit reveals 2.11 ns lifetime for Dil(3) and 3.99 ns lifetime for Nile Red.

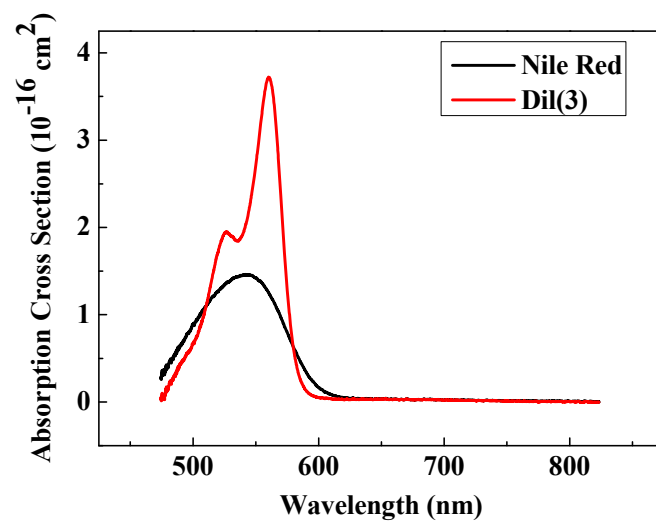


Fig. S5 Absorption cross section of Nile Red and Dil(3) based on absorbance test with 7.5 μM solutions.

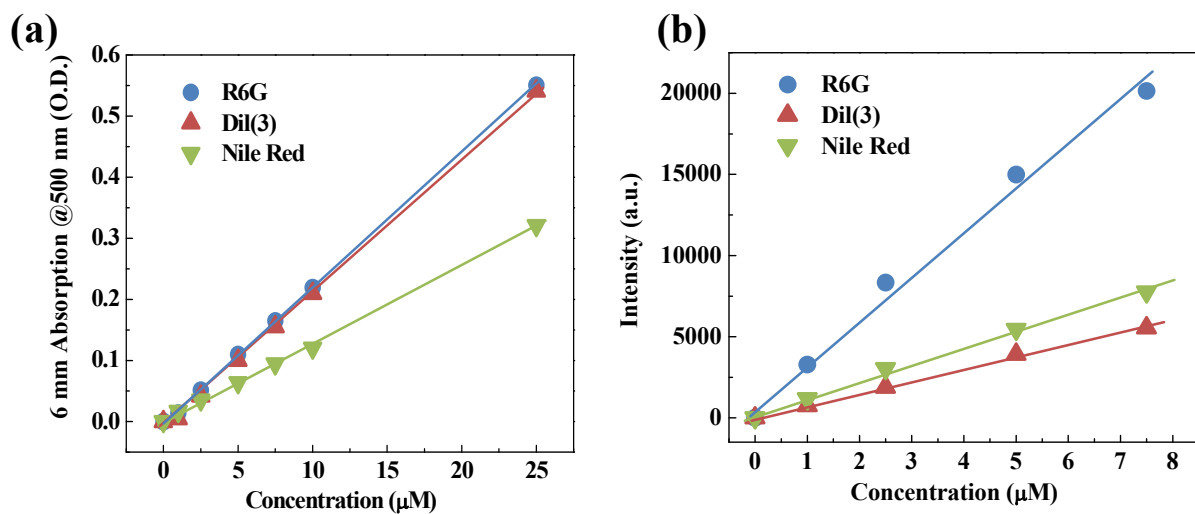


Fig. S6 (a) Absorbance of R6G, Dil(3), and Nile Red at 500 nm. (b) Integrated fluorescence intensity vs. concentration for R6G, Dil(3), and Nile Red. Integration is taken over a 270 nm span between 480-750 nm for R6G and 530-800 nm for Dil(3) and Nile Red.

Table. S1 Extinction coefficient (ϵ) and fluorescence efficiency (FL-slope) for each dye.

Dyes	Extinction (ϵ)	FL-Slope	RI
R6G/MeOH	$3.66 \times 10^4 \text{ M}^{-1} \text{ cm}^{-1}$	$2827.17 \mu\text{M}^{-1}$	1.3284 (methanol)
Dil(3)/ImOil	$3.57 \times 10^4 \text{ M}^{-1} \text{ cm}^{-1}$	$753.38 \mu\text{M}^{-1}$	1.516 (immersion oil)
Nile Red/ImOil	$2.12 \times 10^4 \text{ M}^{-1} \text{ cm}^{-1}$	$1064.89 \mu\text{M}^{-1}$	1.516 (immersion oil)

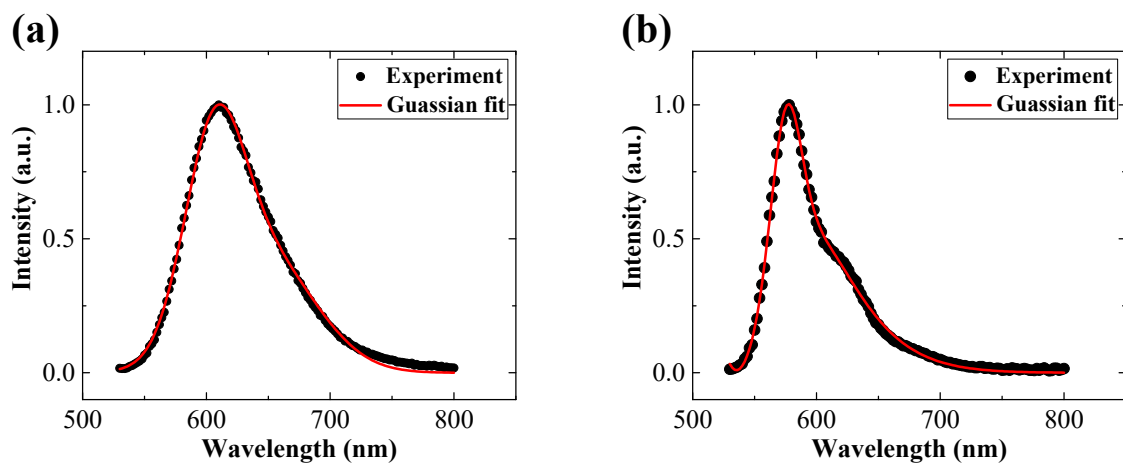


Fig. S7 (a) Nile Red fluorescence spectrum. Gaussian fit reveals 610 nm center wavelength and 43.16 nm standard deviation. (b) Dil(3) fluorescence spectrum. Gaussian fit reveals 578 nm center wavelength and 40.45 nm standard deviation.